Sustainable Energy & Fuels

Design Principles of Tandem Cascade Photoelectrochemical Devices

Journal:	*Sustainable Energy & Fuels*
Manuscript ID	SE-ART-08-2021-001322.R1
Article Type:	Paper
Date Submitted by the Author:	23-Oct-2021
Complete List of Authors:	Kong, Calton; University of California Berkeley, Materials Science Department; Lawrence Berkeley National Laboratory, Chemical sciences Division Warren, Emily; National Renewable Energy Laboratory Greenaway, Ann; National Renewable Energy Laboratory, Materials Chemistry & Computational Science Prabhakar, Rajiv Ramanujam; Lawrence Berkeley National Laboratory, Chemical sciences division Tamboli, Adele; National Renewable Energy Lab, ; Colorado School of Mines, Physics Ager III, Joel; Lawrence Berkeley National Laboratory, Materials Sciences

Design Principles of Tandem Cascade Photoelectrochemical Devices

Calton J. Kong,[†,#] Emily L. Warren,[¶] Ann L. Greenaway,[¶]

Rajiv Ramanujam Prabhakar,[†,#] Adele C. Tamboli,[¶] and Joel W. Ager[†,‡,Δ]

[†]Liquid Sunlight Alliance, [#]Chemical Sciences Division, [‡]Materials Sciences Division, Lawrence Berkeley National Laboratory, California 94720, United States

[Δ]Department of Materials Science and Engineering, University of California, Berkeley, California 94720, United States

[¶]Liquid Sunlight Alliance, National Renewable Energy Laboratory, Golden, Colorado 80401, United States

Corresponding Author

[*]Joel W. Ager

KEYWORDS: Cascade catalysis, photoelectrocatalysis, CO_2 reduction

ABSTRACT. Cascade photoelectrocatalysis (PEC) is a possible method to improve the selectivity of solar-driven CO_2 reduction (CO_2R). This concept can be realized by coupling different CO_2R catalysts to different subcells in a multijunction photovoltaic (PV) stack. Efficient implementation will require careful tuning of the photocurrents and design of the photovoltages provided by the subcells to the CO_2R catalysts in such a way as to facilitate the target reaction. Here, we outline the design principles of the tandem PEC approach using two-step conversion of CO_2 to ethylene in aqueous electrolyte, via a CO intermediate, as a model system. To perform this reaction, the first coupled PV-catalyst component should provide 4 electrons to reduce 2 molecules of CO_2 to CO; the second component should provide 8 electrons to reduce 2 CO molecules to C_2H_4. Based on known CO_2R catalysts, the overpotential required to produce CO can be less than that required to reduce it to ethylene, creating the opportunity for improved efficiency. Cascade PEC can be realized in a three-terminal tandem (3TT) configuration using III-V-semiconductor based subcells coupled to Au (produces CO intermediate) and Cu (converts CO to ethylene). The current to each catalyst can be controlled by the area of the subcell exposed to the electrolyte, and the photovoltage is determined by the materials selected and device configuration. Operating conditions are found by simulating the coupled system using the open-source circuit simulator SPICE (Simulation Program with Integrated Circuits Emphasis). We identify conditions under which a 3TT configuration can have a higher solar to chemical conversion efficiency compared to a two-terminal two-junction tandem (2T 2J) with the same absorbers and a Cu catalyst only. We also show that 3TT PEC devices can be less sensitive to variations in catalyst activity compared to 2T devices. Finally, we discuss the applications of cascade PEC to CO_2 reduction, using different intermediates, and to other chemical networks.

1. INTRODUCTION

Photocatalysis and photoelectrocatalysis are of interest to a number of technologies associated with sustainability including waste remediation,[1,2] upcycling of plastics,[3,4] solar water splitting,[5–8] and solar carbon dioxide reduction.[9–12] Some of the underlying chemical transformations associated with these processes are comparatively simple: for example, in water splitting there are limited pathways for unwanted byproducts and separation is simplified by the fact that the products are insoluble gases. In other cases, selective generation of the target products remains an unmet challenge. In nearly all forms of prospectively sustainable CO_2 reduction operating near room temperature – photocatalytic, electrocatalytic, and photoelectrocatalytic – it is currently not possible to make a single, separable, product with high yield and selectivity.[13–20]

Focusing on electrocatalytic (EC) and photoelectrocatalytic (PEC) reduction of CO_2 (CO_2R), most studies employ a single catalyst biased at a single potential during operation, with significant attention paid to the structure and environment of the active site, the binding energies of key intermediate species and the activation barriers between them, and the management of the fluxes of reactants and products.[21–23] However, in biological processes such as the oxidation of carbohydrates in respiration or their formation in photosynthesis, reaction networks consisting of cascades of individual steps are used to produce products selectively, avoiding deleterious by-products.[24,25] With this concept as inspiration, CO_2R cascades have been reported using homogeneous catalysts and H_2 or NADPH as the reductant,[26,27] and coupling of PEC CO_2R with enzymes has been proposed as a pathway to C_3 and higher order products.[28] Recently, a number of studies have investigated tandem cascade EC-CO_2R using bimetallic catalysts, often coupling a CO-producing metal such as Ag with Cu, which is capable of producing C_{2+} products using either CO or CO_2 as a precursor.[29,30,39,31–38] This concept has also been used in flow reactors and tandem

cascade Ag-Cu catalysts have been integrated with photocathodes to perform overall, solar-driven CO_2 reduction with modest conversion efficiency.[40–42]

Critically, the individual electrocatalysts in the cascade EC and PEC CO_2R studies mentioned above were operated at a single potential. Given that the products of EC-CO_2R can vary widely with the applied potential, the question naturally arises as to whether selectivity could be employed by operating the constituent electrocatalysts in the cascade at different potentials. It is generally agreed that CO is an intermediate for CO_2 reduction to C_2 products on copper,[43] and it is also known that CO conversion on Cu requires a lower overpotential than CO_2 conversion on Cu.[44] This suggests that coupling a CO-producing catalyst operated at a different, lower potential could lead to increases in energy conversion efficiency for C_{2+} products.

This paper explores the design principles of a PEC system which allows the catalysts in a tandem cascade to be operated at different potentials. We show that three-terminal tandem (3TT) photovoltaic (PV) devices, which can provide different photovoltages and photocurrents at different cell contacts, depending on the device geometry and measurement configuration,[45] allow this concept to be realized. We examine a model system of CO_2 reduction to ethylene through a CO intermediate to illustrate the use of 3TT PEC devices for CO_2R. Experiments have shown low overpotentials required to reduce CO_2 to CO on Au nanoparticles.[46] Thus, coupling a Au-based catalyst to the middle (Z) contact could take advantage of the low overpotential by first reducing CO_2 to CO in a low potential region then proceeding to reduce the CO in another region of higher potential using a Cu-based catalyst.

First, we propose a model 3TT PEC system in a configuration that has voltage additivity like a normal tandem but can split the currents between a 1J and 2J region, which is suitable for driving a two-step tandem cascade, and calculate the current density in each of the subcells as a function

of applied bias. We show that for CO_2 conversion to ethylene through a CO intermediate, this device could have a higher solar to chemical conversion efficiency compared to single catalyst devices on either single or tandem absorbers depending on electrochemical behavior and selectivity. Next, we show how the design can be optimized for specific catalyst activities by adjusting the effective areas of the subcells. Finally, we outline the principles and design for 3TT PEC devices in general and discuss possible applications to CO_2 reduction using different intermediates and to other chemical networks as well as looking into the time domain.

2. RESULTS

2.1 Simulation overview.

Our model focuses on the electrical and catalytic behavior of a 3TT device, and for simplicity does not include mass transport or thermal effects. The specific configurations we simulate are shown schematically in Figure 1. Figure 1a shows the 3TT model system of interest while Figures 1b and 1c show the two-terminal (2T) comparisons: a two terminal 2 junction (2T 2J) and a two terminal 1 junction (2T 1J), respectively. Experimental realizations of the 2T-2J configuration for CO_2 reduction have been reported previously and are summarized in Table S1 of the ESI.

For the 2T cases, the single junction device has one GaInP PV component, and the two-junction device has two PV components, GaInP and GaAs, connected in series for voltage additivity. These subcells are current matched and have equal area. Holes collected at the p-type top contact (T) can drive water oxidation at the counter electrode. In the 2T configurations, electrons can be extracted to drive reduction reactions in solution at the n-type back contact (R). For these simulations, a Cu-like CO_2 reducing catalyst will serve as the back contact.

For the 3TT case, using nomenclature developed by Warren et al,[45] the schematic shown in Figure 1a is "GaInP/s/GaAs(p/n) 3TT," designating a series connection of two cells with p/n polarity for both cells. The photovoltaic elements are GaAs (bottom cell) and GaInP (top cell) where top/bottom refer to the order in which the cells absorb light. For the 3TT, as shown in Figure 1a, the GaAs has a smaller area than the GaInP, allowing for current splitting with the middle contact. Electrons can be extracted at the n-type middle contact (Z) from the GaInP and at the n-type back contact (R) from the GaAs, with the potential at the latter contact being more negative. This contact configuration is analogous to a "common T" or CT test configuration from Warren et al, as the T contact is shared as the counter electrode.[45] The CT configuration generates the highest voltages at the remaining two contacts (R and Z). In this configuration, all of the photocurrent passes through the GaInP top cell, which is split between the middle and bottom contacts. For the simulations, a Au-like CO producing catalyst was placed on the GaInP contact and a Cu-like CO reducing catalyst was placed on the GaAs.

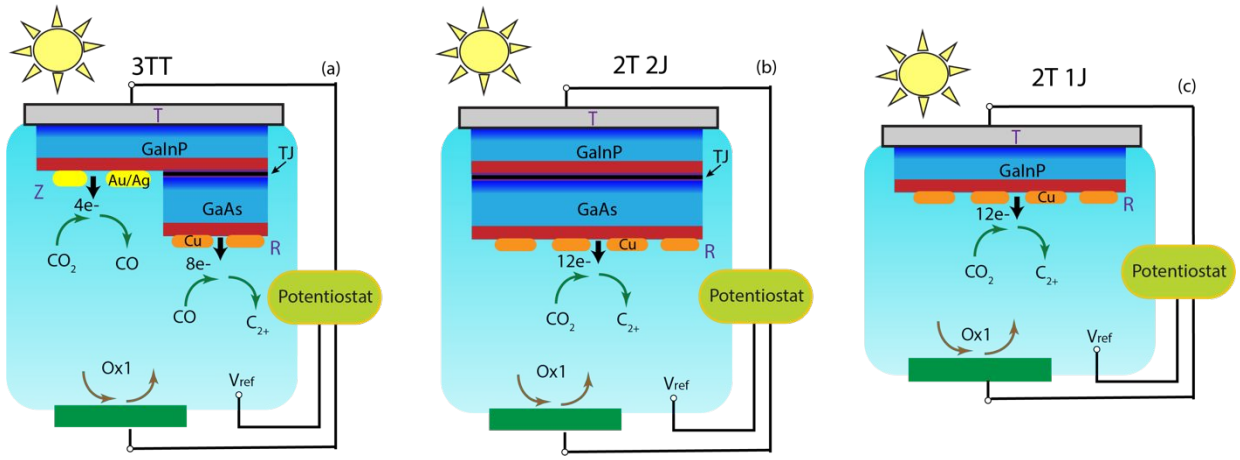

Figure 1: (a) Schematic of a GaInP/s/GaAs (p/n) three terminal tandem (3TT) PEC device. Blue shading indicates p-type doping, red shading indicates n-type doping, and the cells are connected in series using a tunnel junction (TJ). Catalysts are coupled to the n-contacts of both sub-cells: Au (yellow) is the middle contact (Z) and Cu (orange) is the bottom contact (R). Holes are extracted

from the top (T) contact to drive the oxidation reaction at the counter electrode. (b) Schematic of 2T 2J cell with same absorbers as (a) with a copper bottom contact. (c) Schematic of 2T 1J cell with a GaInP absorber with a copper bottom contact. An image of experimental PEC cell which could be used to realize concept in (a) is shown in the ESI, Figure S1.

Two-step conversion of CO_2 to ethylene proceeds through the following two electrochemical half reactions:

$$2\ CO_2 + 4\ H^+ + 4\ e^- \rightarrow 2\ CO + 2\ H_2O,\ E^0 = -0.104 \text{ vs. RHE} \quad (1)$$

$$2\ CO + 8\ H^+ + 8\ e^- \rightarrow C_2H_4 + 2\ H_2O,\ E^0 = +0.170 \text{ vs. RHE} \quad (2)$$

At the same time, Cu is capable of C_2H_4 production directly from CO_2, without externally supplied CO:

$$2\ CO_2 + 12\ H^+ + 12\ e^- \rightarrow C_2H_4 + 4\ H_2O,\ E^0 = +0.08 \text{ V vs. RHE} \quad (3)$$

We refer to reactions 1 and 2 as the cascade mechanism and we refer to reaction 3 as direct conversion. As an illustrative base case, the total current density-voltage behavior of Au (reaction 1), and COR (reaction 2) and CO_2R (reaction 3) on Cu were simulated by assuming Butler-Volmer kinetics based on the reports of Jouny *et al.*,[39] Li *et al.*,[47] Chen *et al.*,[46] and Gurudayal *et al.*,[11] as shown Figure S2. Importantly, in these reports, the onset potential for CO_2 reduction to CO on Au is less negative (kinetically more favorable/occurring at a lower overpotential) than CO reduction on Cu (-0.15 V compared to -0.45 V). The current densities used in the simulations (0-14 mA cm^{-2}) map onto experiments performed in near-neutral pH in CO_2-saturated water; these current densities are conservative estimates of typical 1-sun short circuit current densities of GaInP/GaAs tandem solar cells.[48] For both catalysts, we will neglect the competing hydrogen evolution reaction (which can have a faradaic efficiency (FE) as low as 10% on Cu) such that all current is used for CO_2 reduction;[49] assumptions regarding the faradaic efficiencies to the different C-containing products

will be discussed below. We also assume that the CO produced at the Au catalyst will be available for further conversion at the Cu; prior experimental work has shown this diffusion or convective-mediated pathway can be very efficient.[31,41] Throughout the paper, we assume a 1 cm^2 electrode area, and reduce the GaAs area proportionally to vary the current ratios.

The equivalent circuits of the schematics shown in Figure 1 are shown in Figure S3. Because the potential between the cell's T contact and the reference is set by the potentiostat and the R and Z contacts are constrained to each other via the solution, the cell's behavior can be represented as a single *I-V* curve (contrary to a contour plot for a 3TT photovoltaic device) which we simulated using a SPICE circuit simulator (see SI for more simulation details). When configured in a two terminal tandem (2T 2J) configuration, a GaInP/GaAs tandem typically has a J_{sc} value of 14 mA cm^{-2} with a V_{oc} of 2.5 V, with the GaInP cell being current limiting.[48] For a 3TT configuration, the current matching condition is relaxed as the top cell current can be split between the middle (Z) and bottom (R) contacts. As a starting point for the simulation of a 1 cm^2 cell, we assumed that the GaInP cell has a 1-sun I_{sc} of 12 mA and a V_{oc} of 1.4 V, and that the GaAs (with an illuminated area of 0.625 cm^2) cell has an I_{sc} of 7.5 mA and a V_{oc} of 1.0 V.

In our model, we tune the currents of the subcells by varying their generation currents, which is representative of changing their areas/thickness or varying the spectral conditions. For this work, the I_{sc} of the GaAs cell will be adjusted by varying its area proportionally to a current density of 12 mA cm^{-2} (7.5 mA corresponds to 0.625 cm^2). Thus, in the 2T 2J case, the areas will be equal and current matched. Given the current densities predicted by the SPICE simulations, product production rates were calculated based on expected faradaic efficiencies for Au and Cu catalysts. While Au is selective for production of CO, the CO_2R/COR product distribution produced by Cu depends strongly on potential. Moreover, on Cu the onset potential for reaction (2), CO reduction

to C_2H_4, is known to be less negative than reaction (3), CO_2 reduction to the same product. As will be shown in Section 2.2, for the base case 3TT design (Figure 1a) the potential range in which both catalysts are producing products corresponds to the potential range where the 2J/Cu region is operating at its light-limited current. For the base case simulation of the 3TT, we capture the improved performance of COR by increasing its faradaic efficiency toward ethylene (85% for COR and 50% for CO_2R). In Section 2.5 we will discuss how this behavior changes as we vary the activity of CO_2R relative to COR.

Table 1: Summary of the parameters used for the base case simulation of a 1 cm^2 3TT PEC cell. More details about the PV model inputs are in Table S2 and 1-sun *J-V* curves are in Figure S4.

(Sub)Cell	I_{sc} (mA)	Area (cm^2)	V_{oc} (V)	Fill Factor	FE (%)	Dark Onset (V vs RHE)
GaInP/Au	12	1	1.4	0.88	CO: 100	-0.15 (CO_2 -> CO)
GaAs/Cu	7.5	0.625	1.0	0.85	C_2H_4: 85 (COR) C_2H_4: 50 (CO_2R)	-0.45 (COR) -0.65 (CO_2R)

2.2 Simulation results.

We first simulate the *I-V* behavior of the two-terminal devices to establish a comparison. The *I-V* behavior of the reduction half-cell in the 2T configurations are shown in Figure 2. Onset of photocurrent occurs at +1.75 V vs RHE, and comparison of the dark and light curves in Figure 2a shows that the solar cell provides about 2.4 V as seen by the onset difference between the light and dark curves. This shows the voltage additivity seen in tandem PV. The ethylene curve represents the partial current toward ethylene, and because the assumed faradaic efficiency to ethylene is 50% this curve is simply half the photocurrent. For the 2T 1J case shown in Figure 2b, the photocurrent onset is at +0.75 V vs RHE, showing that the solar cell only provides 1.4 V as expected because there is only one photoabsorber to generate voltage. The low voltage and high overpotentials for CO_2R on Cu make the 2T 1J configuration less favorable; the 2T 2J case does provide significantly

greater voltage, but the chemical reaction proceeds via a less selective pathway (reaction 3). Thus, we simulate the 3TT case, which we expect to enable the cascade mechanism, taking advantage of greater selectivity and lower overpotentials for CO_2R on Au.

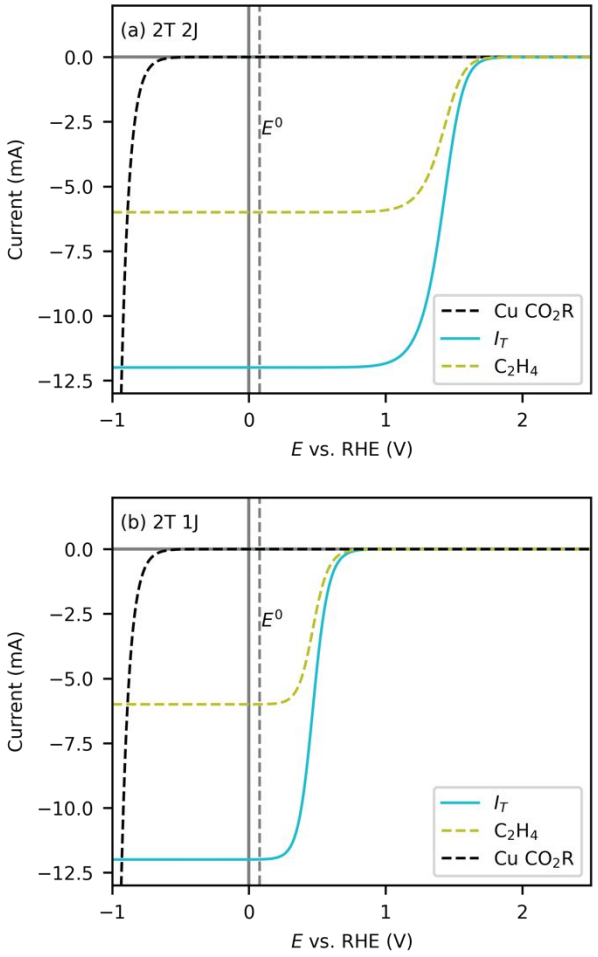

Figure 2: (a) Current density-voltage (*I-V*) behavior for the 2T 2J device shown schematically in Figure 1b using parameters described above: cyan, I_T. E^0 for CO_2R to ethylene (dashed grey line), reaction (3), and the assumed *I-V* behavior of Cu in the dark, i.e. without being coupled to solar cells (dashed black line). The dashed yellow curve is the partial current density to ethylene. (b) Current density-voltage (*I-V*) behavior for the 2T 1J (GaInP) device shown in Figure 1c using parameters described above.

We simulate the *I-V* behavior of the 3TT PEC CO_2 reduction half-cell (Figure 3a) using the parameters summarized in Table 1. Note that in a physical experiment, the potentiostat would measure I_T or the total current (blue curve), but the simulation allows us to access the subcircuit behavior. The behavior of the coupled cells is best discussed starting at the point of current onset, which is +1.75 V vs. RHE, the same as with the 2T 2J case. As the potential is swept to more negative values, initially, all the current goes through both cells to the Cu catalyst (green trace for Cu overlaps the blue curve for the total current density); that is, $I_{TZ} = 0$. The current onset for cascade conversion is at +1.25 V vs. RHE where CO production starts from the Au connected to the GaInP cell, allowing the copper contact to begin converting CO via reaction (2). The total current density reaches the current limit set by the GaInP cell, -12 mA cm^{-2}, at +0.9 V vs RHE.

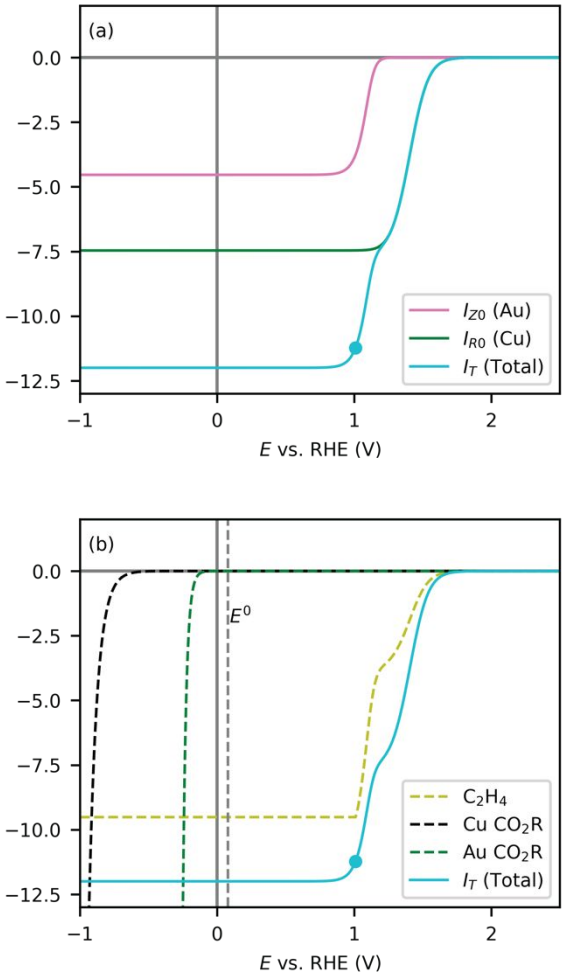

Figure 3: (a) Current density-voltage (*I-V*) behavior for the 3TT schematic shown in Figure 1a using the parameters in Table 1: pink, I_{Z0} (GaInP/Au), green, I_{R0} (GaInP/GaAs/Cu); cyan, I_T (total) (note that the total curve and the GaInP/GaAs/Cu curves overlap for *E* greater than +1.25 V vs RHE). The cyan circle is the cascade operating point, discussed in the text. (b) Chemical behavior of the cell, E^0 for CO_2R to ethylene (dashed grey line), reaction (3), and the assumed *I-V* behavior of Cu and Au in the dark, i.e. without being coupled to solar cells. The dashed yellow curve is the partial current density to ethylene.

The partial current density to ethylene is shown in the yellow trace in Figure 3b. When only the Cu pathway is operating via reaction (3), from +1.75 to +1.25 V vs RHE, ethylene is half the total

current density corresponding to the assumed FE of 50% (Table 1). However, the ethylene partial current density increases sharply in magnitude when the cascade mechanism becomes possible at +1.25 V vs RHE. Its limiting value is -9.5 mA cm^{-2} for potentials of 1.05 V and below; in this potential range the CO_2 reduction to ethylene proceeds completely through the cascade mechanism (reactions 1 and 2).

The cascade operating point, indicated as a cyan dot in the figures, is defined as the most positively biased point where all ethylene production proceeds by the cascade mechanism. At this point, the faradaic efficiency for ethylene is at its maximum and the net production of CO is zero (Figure S5). As discussed in Section 2.3, the cascade operating point in this case also corresponds to the maximum solar conversion efficiency for production of ethylene. Further reducing the bias past the cascade operating point increases CO production, but not ethylene, decreasing the faradaic efficiency of ethylene (Figure S5).

Figure 3 reveals additional details of the behavior of the coupled subcells. The GaInP cell supplies the current for both cells, hence the I_{sc} for the GaInP cell is the total limiting current. The GaAs cell determines the distribution of current as the I_{sc} for the GaAs cell is the limiting current for the Cu catalyst (there are exceptions to this which will be discussed in Section 2.5). The V_{oc} for the GaInP/GaAs tandem can be seen as the difference between the onset of the dark curve for Cu (dashed line) and the onset of the cyan/green curve at +1.75 V vs. RHE. The V_{oc} for the GaInP cell by itself is the difference between the current onset for the Au catalyst in the dark (-0.15 V vs RHE, Figure 3) and the Au curve (red) in Figure 2. The cascade operating point (cyan dot) depends on the overpotential for the Au catalyst; a lower overpotential would shift this point to more positive values. As will be discussed in Section 2.6, the cascade operating point is comparatively less sensitive to the overpotential for the Cu catalyst.

2.3 Solar to chemical conversion efficiency.

To determine optimal parameters for cell design and operation and to assess trade-offs, we use the applied bias photon-to-current (Φ_{ABPC}) efficiency:[50]

$$\Phi_{ABPC} = \frac{\Delta G_{product} \cdot \frac{J}{nF} \cdot (\mathrm{FE}) - J(E - E^0)}{P_{sun}} \quad (4)$$

where ΔG is the free energy change for the reduction half reaction, n is the number of electrons transferred, J is the current density (normalized to the GaInP cell area), F is faraday's constant, FE is the faradaic efficiency toward the product, E is the operating potential, E^0 is the standard reduction potential for the half reaction, and P_{sun} is the solar intensity. This metric captures the difference between the power going to the target chemical minus any added electrical power and is normalized to the incident light intensity. It can also be thought of as the theoretical maximum solar to chemical conversion efficiency of the full cell in the limit of zero overpotential for the water oxidation reaction at the counter electrode. Graphically, Φ_{ABPC} will be positive for regions of the *I-V* curves where the partial current density for ethylene is negative and the power generated from the positive bias is greater than energy decrease from the downhill half reaction.

Φ_{ABPC} as a function of applied bias is shown in Figure 4a assuming a 1-sun AM1.5G intensity of 100 mW cm^{-2}. Data for the base case ethylene FE (85%) (Table 1) for the COR reaction is shown as well as data for smaller and larger values. Starting at positive values of the bias voltage and sweeping to more negative values, Φ_{ABPC} becomes positive at +1.75 V vs RHE, corresponding to the onset of ethylene production by the Cu catalyst driven by both cells. For the base case (Table 1), the Φ_{ABPC} for direct conversion of CO_2 to ethylene reaches 4% at +1.3 V vs RHE. Φ_{ABPC} increases sharply when the cascade mechanism becomes possible at +1.25 V vs RHE. The maximum conversion efficiency reaches 8.3% at E = 1.05 V vs. RHE for 85% FE; this point is the

cascade operating point in Figure 3a and is a condition which is similar to the maximum power point (MPP) of a solar cell. At more negative bias, Φ_{ABPC} decreases linearly (Figure 4a, dashed line).

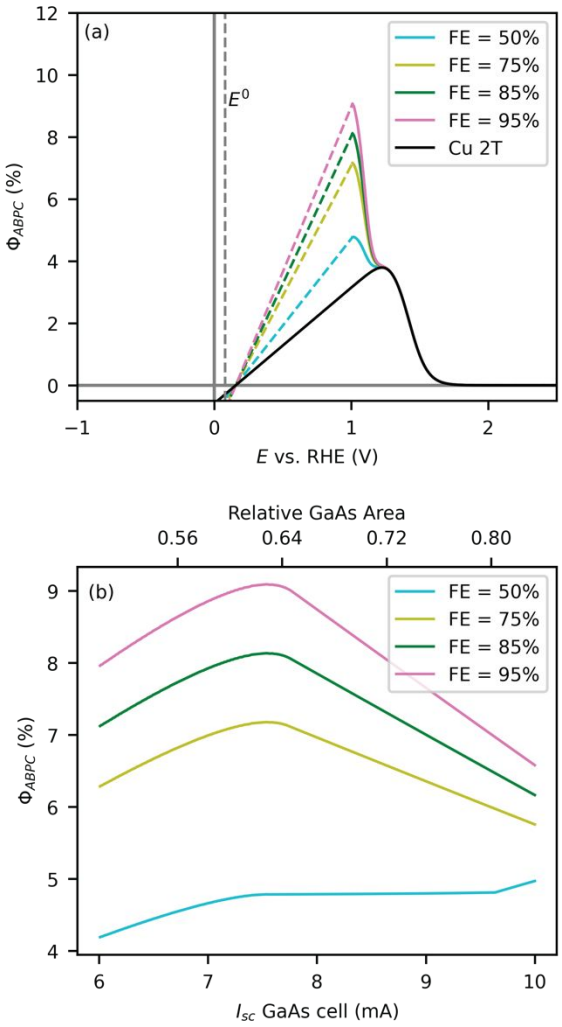

Figure 4: (a) Φ_{ABPC} for ethylene production (Eq. 4) for the 3TT cell shown in Figure 1a, the GaInP/GaAs/Cu cell only (black, $I_{TZ} = 0$), and for different values for the FE for CO conversion to ethylene (50-95%). Dashed lines indicate the region where there is no further ethylene production with decreasing potential. (b) Maximum Φ_{ABPC} as a function of I_{sc} of the GaAs cell (adjusted by changing area) for different faradaic efficiencies for CO conversion to ethylene (50-

95%). The total limiting current for the cell was set at 12 mA as defined by the 1 cm^2 GaInP top cell.

There are two interesting features in Figure 4a. First, we note the sharp drop in Φ_{ABPC} at +1.05 V vs RHE for cascade mechanisms regardless of assumed FE. This is due to ethylene production being determined by the current available to the Cu catalyst; if more CO is produced than Cu can reduce to ethylene, it is not possible to convert it. Therefore, for potentials more negative than the point of maximum Φ_{ABPC}/cascade operating point, the additional CO produced is not converted to ethylene and the ethylene current saturates, leading to the linear decrease in Φ_{ABPC} in this region. (as shown by the dashed lines in Fig 4a). Secondly, the small dip between +1.2 V and +1.3 V is due to the saturation of the photoabsorber current going to the Cu contact before the onset of CO production. In this region, the copper current (I_R) does not increase with decreasing potential, which is expected for a semiconductor photoelectrode, causing decreased efficiency in that region. We can see this by superimposing the Φ_{ABPC} of the $I_{TZ} = 0$ case (all current flows through the GaInP and GaAs components to the rear Cu (R contact)) on top of the total Φ_{ABPC} in this region (red curve). This fact will be useful in Section 2.6 when discussing the sensitivity of these cells to variations in catalyst overpotential.

For the base case (Table 1), we find that the maximum Φ_{ABPC} occurs when the partial current density for CO produced by the Au (Z contact) is half that of the current of Cu (R contact) such that all ethylene is produced by a cascade of reactions 1 and 2. At this point, the copper contact has already reached current saturation; although more negative applied potentials would increase (slightly) the CO production, it would not be converted to ethylene and maximum Φ_{ABPC} would not increase. Notably, changes in the faradaic efficiency of ethylene production by COR (reaction 2) change the value of the maximum Φ_{ABPC} but do not change the cell bias at which it occurs. If

COR is assumed to have the same ethylene FE as CO_2R (50%), operating in the cascade region (E < 1.25 V vs RHE) is still favorable as the ethylene current still increases, despite there being no selectivity advantage (cyan dashed line, Figure 4a). We will see that the case of 50% FE is not advantageous compared to 2T 2J tandems in the next section.

The relative area of the GaAs cell, which sets I_{sc}, is an important design parameter. Figure 4b shows the maximum Φ_{ABPC} as a function of the I_{sc} of the GaAs cell while maintaining the I_{sc} of GaInP at 12 mA (for a 1 cm^2 device). For the base case FE for CO conversion to ethylene (85%), the maximum Φ_{ABPC} occurs when the GaAs I_{sc} is 7.56 mA, which is close to the 7.5 mA used in the base case (Table 1). This optimal value for GaAs I_{sc} is unchanged for COR to ethylene FE values between 75% and 95%. However, if the FE for COR to ethylene decreases to 50% (cyan curve), there is not a clear maximum. As discussed in Section 2.4, there is no longer an energy conversion advantage of the 3TT compared to the 2T 2J in this case.

2.4 Comparison of 2T and 3TT geometries.

The Φ_{ABPC} metric is useful to compare the 3TT to the 2T configurations. Φ_{ABPC} as a function of bias at different faradaic efficiencies for COR to ethylene for the 2T 2J and 2T 1J cases are shown in Figure 5a and b. Using the base case values (Table 1), the maximum Φ_{ABPC} values are 5.9% and 1.1% for the 2T 2J and 2T 1J cases, respectively, which are lower than the 8.3% value for the 3TT case. Thus, the use of 3TT-mediated cascade pathway makes the overall conversion of CO_2 to ethylene more energy efficient compared to similar two terminal devices under the base case assumptions (Table 1).

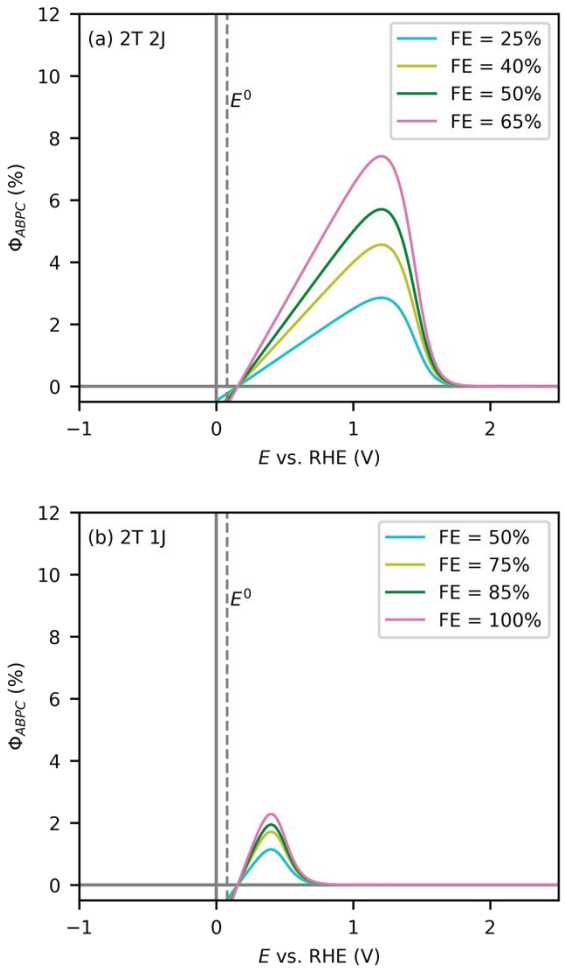

Figure 5: (a) Φ_{ABPC} vs E for the 2T 2J device at varying faradaic efficiencies for CO_2 to ethylene. (b) Φ_{ABPC} vs E for the 2T 1J device at varying faradaic efficiencies

This analysis allows determination of conditions for which a 3TT design will be more efficient than other geometries. Comparing to a single absorber geometry is quite simple. Even assuming 100% faradaic efficiency for the direct conversion of CO_2 to ethylene, the GaInP single absorber configuration has a maximum Φ_{APBC} of 2.3%, which is lower than that of the 3TT configuration. This is because the 3TT's cascade operating point is at higher potentials compared to the potential at max Φ_{APBC} due to the lower overpotential of CO production compared to direct CO_2 reduction.

Comparison to the 2T 2J case is more nuanced and depends on catalyst selectivity and activity, both of which might be improved in the future. Although the maximum Φ_{APBC} for the 2T 2J case occurs at higher potentials, they also suffer from the low faradaic efficiencies and higher overpotentials of CO_2R on Cu, which means their performance compared to 3TTs will be very sensitive to the catalyst performance. The 3TT mediated cascade mechanism needs to be more faradaically efficient than the 2T 2J mediated direct conversion to be equally or more efficient. In the base case, the FE for cascade conversion (3TT mediated) would need to be 60% to be equally efficient with direct conversion (2T 2J mediated) which has 50% FE. Thus, under the current assumptions, it only takes a modest selectivity gain for the 3TT to be more efficient. These increases in selectivity for COR compared to CO_2R have been shown before.[39]

2.5 Response to varying Cu CO_2R overpotential.

In our analysis above, we examined the case when the CO_2R onset (-0.65 V vs RHE) is more negative than that for COR (-0.45 V vs RHE). However, the range of experimentally reported overpotentials for CO_2R is quite large, motivating us to consider how 3TT tandem PEC cells can be designed for different values of this parameter. To this end, we will consider two limiting cases: one where CO_2R and COR have the same (modest) onset and one where the CO_2R overpotential is very large (resulting in Cu onset more negative than Au onset), anticipating that intermediate cases will lie between these two extremes. Figure 6a shows the *I-V* behavior of 3TT PEC cell configuration shown in Figure 1a, but with the dark CO_2R onset and COR onset both at -0.45 V. Figure 6b shows the *I-V* behavior in identical conditions except with dark COR onset at -0.45 V and dark CO_2R onset at -1.5 V.

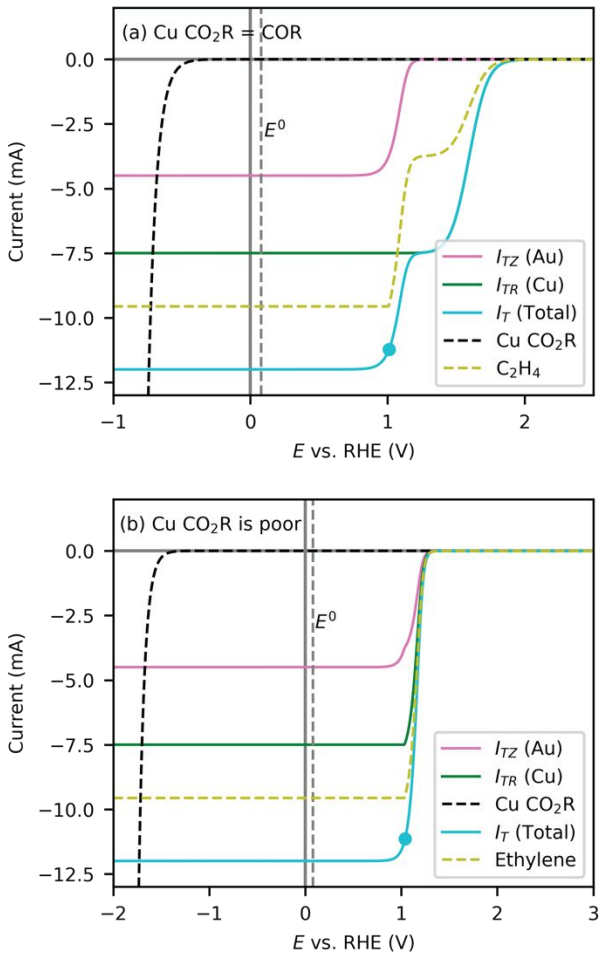

Figure 6: (a) *I-V* behavior for 3TT device in the case where COR and CO_2R onset potentials are both -0.45 V vs RHE (all other parameters are the same as Table 1). (b) *I-V* behavior for 3TT device in the case where CO_2R onset is much lower than COR.

In Figure 6a, we see that the *I-V* behavior is similar, overall, to the base case (Table 1). The only difference is that the copper catalyst (R contact) saturates at higher applied bias prior to cascade onset, which allows for greater efficiency outside the cascade region ($E > 1.25$ V vs RHE). Figure 6b depicts an extreme case of CO-limited ethylene production due to the very large overpotential for the direct CO_2 conversion pathway on Cu. Thus, in this case, CO production from the Au catalyst and ethylene production from the Cu catalyst begin at the same applied bias, +1.25 V vs RHE. In principle, a direct CO_2 to ethylene pathway would be possible at +0.9 V vs RHE but

the light-limited current density has already been reached by this point. As the result, there are no conditions of applied bias for which direct CO_2 conversion to ethylene via reaction (3) occurs. Another interesting property arises in these conditions as direct conversion is effectively suppressed. If the I_{sc} for the GaAs cell is increased above 8 mA (by increasing its area), the GaAs subcell would not saturate at that I_{sc} as the CO current would be limiting. The system would instead saturate at 4 mA to the Au (Z) contact and 8 mA to the Cu (R) contact, maintaining a consistent 1:2 ratio of currents such that the Cu is supplied with enough CO to reduce (see Figure S6).

The *I-V* curves for 2T 2J and 2T 1J devices and Φ_{ABPC} vs *E* curves are shown in Figure S7-9 for these limiting cases. Interestingly, the maximum Φ_{ABPC} for the 3TT configuration is similar (ca. 8%) for both of the limiting cases. This shows that a 3TT device can be insensitive to changes in CO_2R activity; further discussion of this phenomenon follows in section 2.6. As expected, the Φ_{ABPC} for a two-terminal cell (2T 1J and 2T 2J) cell depends on the assumed overpotential for direct CO_2 conversion to ethylene via reaction 3, as a cascade pathway is not possible (Figure S9).

2.6 Sensitivity to changes in catalyst activity.

There are significant differences in how 2T 2J and 3TT designs respond to changes in catalyst activity. We consider here the response to an increase in the overpotential for reactions 2 and 3 over time, a phenomenon which is frequently observed experimentally. Figure 7 shows Φ_{ABPC} for ethylene production as a function of the dark Cu overpotential (for both CO_2R and COR), while holding the onset potential of CO_2R to CO on constant. Faradaic efficiencies were chosen (85% for COR and 63% for CO_2R) such that the two cell designs had the same Φ_{ABPC} for a COR/CO_2R onset potential of -0.5 V vs. RHE. For a large range of Cu overpotentials, up to about -0.8 V vs RHE, the position of maximum Φ_{ABPC} for the 3TT device occurs when the Cu catalyst is current limited. As a result, the Φ_{ABPC} for a 3TT device is insensitive to the Cu overpotential over a wide

operating range. In contrast, the Φ_{ABPC} for the 2T 2J design decreases with increasing overpotential (more negative onset potentials), as expected. However, there is a limit to the operating range where the 3TT device outperforms the 2T 2J device. If the Cu overpotential becomes too large, the current tuning requirement for cascade conversion cannot be met and the Φ_{ABPC} for the 3TT device rapidly decreases. In Figure 7, this occurs for onset potentials more negative than -0.85 V vs RHE.

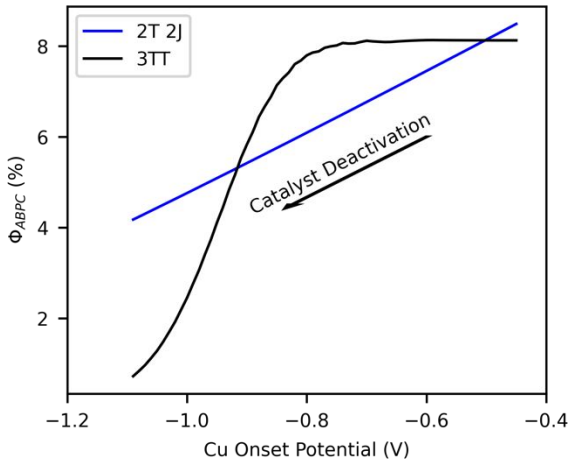

Figure 7: Φ_{ABPC} vs the Cu onset potential for dark COR and CO_2R (with Au onset potential held constant). Faradaic efficiencies were adjusted so curves intersect at two points for illustrative purposes (85% for cascade conversion via reactions 1 and 2 and 63% for direct conversion via reaction 3).

2.7 Design Principles of 3TT PEC devices.

The concept of tandem cascade PEC can be generalized beyond the specific case discussed so far. When designing 3TTs for PEC systems, it is important to choose reactions that can be advantageously done in a cascade with efficient transport of the intermediate species. In the case considered above, the goals were to control selectivity and optimize energy conversion efficiencies, but there could be other motivations, some of which are discussed below.

For each electrochemical step in a cascade, the number of electrons required and their relative standard reduction potential are crucial design parameters as they determine how to couple the electrocatalysts to the PV subcells in order to properly match the photocurrents to the reaction chemistry. A general two-step cascade would have *m* electrons transferred in the first step and *n* electrons in the second step (*m*/*n* was 4/8 for ethylene production through CO):

$$A + m\ e^- + x\ H^+ \rightarrow B + y\ H_2O,\ E^0 = p \quad (5)$$

$$B + n\ e^- + z\ H^+ \rightarrow C + w\ H_2O,\ E^0 = q \quad (6)$$

As an illustrative example on how to design for different reaction chemistries, we will consider a two-step cascade of CO_2 to formaldehyde, then to methanol, with the reduction half reactions and E^0 values shown in equations 7 and 8. This differs from our ethylene case as the difference in the E^0 values is larger and the electron ratio *m*/*n* is 4/2.

$$CO_2 + 4e^- + 4H^+ \rightarrow H_2CO + H_2O,\ E^0 = -0.123\ V\ vs\ RHE \quad (7)$$

$$H_2CO + 2e^- + 2H^+ \rightarrow CH_3OH,\ E^0 = 0.294\ V\ vs\ RHE \quad (8)$$

One could imagine performing these reactions selectively with enzyme or enzyme-like catalysts, such that the faradaic efficiencies are ~100% and the direct 6-electron conversion is not possible. There are experimental reports which suggest that such a system may be possible: Wang *et al*.[27] reported on three step enzyme-mediated conversion of CO_2 to methanol using a micelle microenvironment, and Reda *et al.*[51] have shown that formate dehydrogenase anchored to pyrolytic graphite can reversibly and selectively oxidize/reduce formate/CO_2 at very low overpotentials.

We will assume similar low overpotentials such as those reported by Reda *et al.* for our kinetic models; the *I*-*V* curves for the catalysts in the dark are shown in Figure S10. Because each contact has a different photovoltage it is important to consider where to place each catalyst. In this enzyme example, when the formaldehyde-producing catalyst is coupled to the GaAs (Figure 8a), there is

current at high values of applied potential but no cascade conversion to methanol (this process turns on at applied potentials below +1.6 V vs RHE). In contrast, when the formaldehyde-producing catalyst is coupled to the GaInP sub cell, the methanol enzyme is limited by the formaldehyde current so there is no current for potentials above +1.25 V vs RHE (Figure 8b). Additional parameters for the simulations in Figure 8 are in Tables S3 and S4; Φ_{ABPC} vs E for each simulation are shown in Figure S11 and Figure S12.

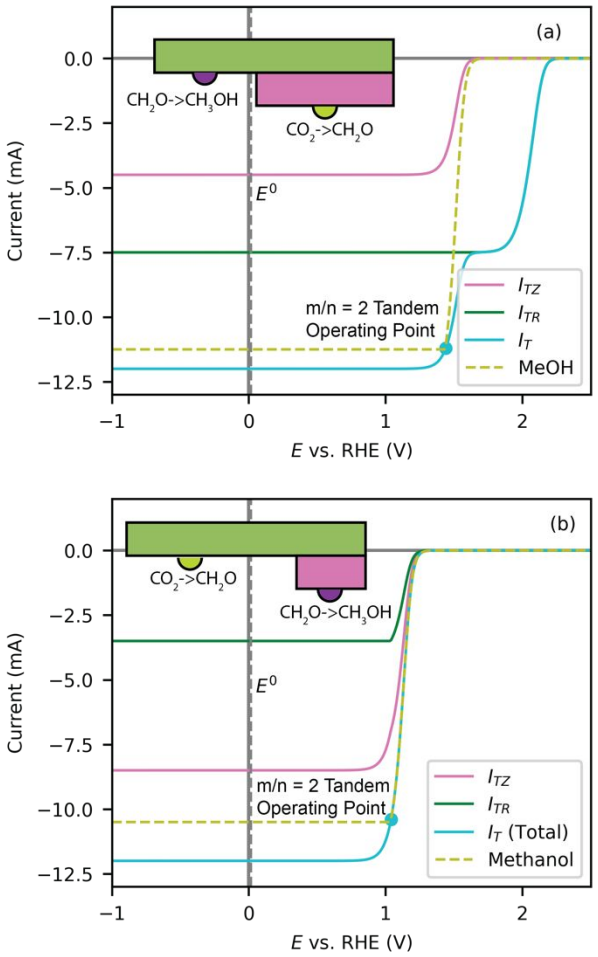

Figure 8: *I-V* behavior of a 3TT cell using enzymes as catalysts: (a) formaldehyde forming catalyst coupled to the GaAs cell and the methanol forming catalyst coupled to the GaInP cell; (b) formaldehyde forming catalyst coupled to the GaInP cell and the methanol forming catalyst coupled to the GaAs cell. Parameters for the simulations are listed in Tables S3 and S4.

The cascade operating point is 0.4 V more positive in Figure 8a than in 8b, making the configuration in 8a more efficient than 8b. As such, when designing 3TT PEC cells, it is generally favorable to couple the catalyst driving the greater (more positive or less negative) E^0/onset to the wider bandgap cell, and the catalyst driving the lower (more negative, or less positive) E^0/onset to the smaller bandgap cell. This maximizes the potential of the cascade operating point relative to E^0 for the full reaction as the wider bandgap subcell determines this value. Coupling catalysts in this manner takes full advantage of the extra voltage from the tandem solar cells. This principle also explains why the Cu cell was coupled to the GaAs absorber in the ethylene production base case (Figure 1a, Table 1) as the onset of CO_2R/COR to ethylene was assumed to be more negative compared to CO generation.

In the insets in Figure 8a and 8b, the relative areas between the two absorbers are also different for each case. In Figure 8a, a larger GaAs cell is needed to increase I_{sc2} for efficient operation, as it drives a process requiring more electrons. However, in Figure 8b, the GaAs cell area must be smaller to decrease $I_{sc2,}$ as it drives a process requiring fewer electrons compared to the other cell (see Figure S13 for case when I_{sc2} was made too large). Tuning the current in this manner optimizes the conversion efficiency toward the desired product and highlights the importance in considering the electron stoichiometry when designing 3TT PEC devices. We consider another case of two-step conversion of CO_2 to ethane via a CO intermediate in Figure S14; in this case m/n = 2/5.

The cascade operating points for all the cases are shown as cyan dots. Following from the discussion in Section 2.2 and 2.3, the cascade operating point maximizes selectivity to the product of the cascade reaction, and for the parameters we have chosen, is also the point of maximum conversion efficiency. Thus, for optimal operation, a system similar to a MPP tracker used in solar cells should be used to maintain operation at the cascade operating point (or point of maximum

efficiency during times when no cascade operating point exists) in response to changes in the spectrum and intensity of the incident light.

3. OUTLOOK

We discuss here two potential extensions of tandem cascade PEC concept: (1) coupling devices together to drive larger chemical network with more electron transfer processes (2) use of the time domain.

To this point, we have considered designs at the cell level; by analogy to coupling PV cells together to form a module, one can consider coupling together different types of cascade PEC devices to drive more complex systems, with cells coupled to different catalysts. An attractive target would be the synthesis of water insoluble products such as hexane or octane as suggested by Yang *et al*.[28] It may be possible to couple electrochemical and thermal conversion steps and/or perform the conversion in a sequence of reactors, as suggested by the tandem electrochemical conversion demonstration of Spurgeon and co-workers.[40]

3TT PEC devices could also be used to affect sequential photocatalysis and perform other time-controlled experiments. One way to do this is using LED mixing, as this allows for optical tuning of the currents. For example, if certain reactions require a higher intermediate concentration before the reaction can proceed, one could maintain a constant blue light to build up intermediate produced at the Z contact and then turn on red light once sufficient intermediate is present. One could also adjust the bias for temporal control of the currents. For example, one could operate at higher potential in the beginning forcing all current through the R contact, then operate at lower bias, turning on the catalyst at the Z contact. The fact that the catalytic sites are spatially separated and, potentially, digitally controllable, could be used to probe transport kinetics or be used for more careful control of selectivity.

4. CONCLUSIONS

In summary, we have outlined design principles for three-terminal tandem photoelectrochemical devices by examining the current tuning requirements for different reaction mechanisms and discussing the systems where using a cascade mechanism would be favorable. We showed that using a three-terminal tandem photoelectrochemical device to drive a tandem cascade reaction is more efficient than a two-terminal single junction device, and depending on the parameters, more efficient than two-terminal two-junction devices for the example case of CO_2R through a CO intermediate. We examined the devices' response to variations in catalyst activity for COR and CO_2R, and showed that three-terminal devices can be less sensitive to variations in catalyst activity compared to the two terminal devices. We also discussed the use of three-terminal tandems for modulated and time-controlled experiments that could open doors toward driving more complex tandem cascade reaction mechanisms and probing reaction kinetics for light driven CO_2 reduction.

5. ASSOCIATED CONTENT

Supporting Information. Simulation methods and supplemental modeling results.

Data availability. Code used in the simulation is publicly available on Zenodo at: https://doi.org/10.5281/zenodo.5593774

Author Contributions. CJK, ELW, ALG, ACT, and JWA jointly conceptualized the paper. CJK, ELW, and JWA worked on the 3T and PEC methodologies, with CJK conducting most of the investigation and analysis, with JWA developing some of the earlier methods, and ELW validating them. CJK and JWA wrote the original draft, with JWA writing the abstract and introduction and CJK writing the results and discussion and outlook. All authors were involved with reviewing and editing the drafts. ACT, ELW, and JWA were involved in funding acquisition and project administration.

ORCID numbers

Calton J. Kong	0000-0003-0313-3565
Emily L. Warren	0000-0001-8568-7881
Ann L. Greenaway	0000-0001-6681-9965
Adele C. Tamboli	0000-0003-2839-9634
Rajiv Ramanujam Prabhakar	0000-0002-4598-9073
Joel W. Ager	0000-0001-9334-9751

Conflicts of interest

ACT, ELW, CJK, and JWA have filed a provisional patent related to the tandem PEC design. The authors declare no other competing financial interests.

ACKNOWLEDGMENT

This material is based on work performed by the Liquid Sunlight Alliance, which is supported by the U.S. Department of Energy, Office of Science, Office of Basic Energy Sciences, Fuels from Sunlight Hub under Award Number DE-SC0021266. This work was supported in part by the U.S. Department of Energy under Contract No. DE-AC36-08GO28308 with Alliance for Sustainable Energy, LLC, the Manager and Operator of the National Renewable Energy Laboratory. The U.S. Government retains and the publisher, by accepting the article for publication, acknowledges that the U.S. Government retains a nonexclusive, paid up, irrevocable, worldwide license to publish or reproduce the published form of this work, or allow others to do so, for U.S. Government purposes. Rajiv Ramanujam Prabhakar acknowledges the Swiss National Science Foundation Early Postdoc Mobility Fellowship (191299) for financial support.

REFERENCES

1 S. Horikoshi and N. Serpone, *Catal. Today*, 2020, **340**, 334–346.

2 S. N. Ahmed and W. Haider, *Nanotechnology*, 2018, **29**, 342001.

3 K. F. Chin, M. Đokić and H. Sen Soo, *Trends Chem.*, 2020, **2**, 485–488.

4 T. Uekert, M. A. Bajada, T. Schubert, C. M. Pichler and E. Reisner, *ChemSusChem*, 2020, cssc.202002580.

5 J. W. Ager, M. R. Shaner, K. A. Walczak, I. D. Sharp and S. Ardo, *Energy Environ. Sci.*, 2015, **8**, 2811–2824.

6 N. S. Lewis, *Science*, 2016, **351**, aad1920.

7 K. Sivula and R. van de Krol, *Nat. Rev. Mater.*, 2016, **1**, 15010.

8 B. Mei, G. Mul and B. Seger, *Adv. Sustain. Syst.*, 2017, **1**, 1600035.

9 J. Rongé, T. Bosserez, D. Martel, C. Nervi, L. Boarino, F. Taulelle, G. Decher, S. Bordiga and J. A. Martens, *Chem. Soc. Rev.*, 2014, **43**, 7963–7981.

10 T. Arai, S. Sato and T. Morikawa, *Energy Environ. Sci.*, 2015, **8**, 1998–2002.

11 Gurudayal, J. Bullock, D. F. Srankó, C. M. Towle, Y. Lum, M. Hettick, M. C. Scott, A. Javey and J. W. Ager, *Energy Environ. Sci.*, 2017, **10**, 2222–2230.

12 F. Urbain, P. Tang, N. M. Carretero, T. Andreu, L. G. Gerling, C. Voz, J. Arbiol and J. R. Morante, *Energy Environ. Sci.*, 2017, **10**, 2256–2266.

13 Y. Hori, in *Modern Aspects of Electrochemistry*, eds. C. G. Vayenas, R. E. White and M. E. Gamboa-Aldeco, Springer New York, New York, NY, 2008, pp. 89–189.

14 S. N. Habisreutinger, L. Schmidt-Mende and J. K. Stolarczyk, *Angew. Chemie Int. Ed.*, 2013, **52**, 7372–7408.

15 J.-P. Jones, G. K. S. Prakash and G. A. Olah, *Isr. J. Chem.*, 2014, **54**, 1451–1466.

16 J. L. White, M. F. Baruch, J. E. Pander III, Y. Hu, I. C. Fortmeyer, J. E. Park, T. Zhang, K. Liao, J. Gu, Y. Yan, T. W. Shaw, E. Abelev and A. B. Bocarsly, *Chem. Rev.*, 2015, **115**, 12888–12935.

17 J. H. Montoya, L. C. Seitz, P. Chakthranont, A. Vojvodic, T. F. Jaramillo and J. K. Nørskov, *Nat. Mater.*, 2016, **16**, 70–81.

18 D. Raciti and C. Wang, *ACS Energy Lett.*, 2018, **3**, 1545–1556.

19 P. De Luna, C. Hahn, D. Higgins, S. A. Jaffer, T. F. Jaramillo and E. H. Sargent, *Science*, 2019, **364**, eaav3506.

20 S. Nitopi, E. Bertheussen, S. B. Scott, X. Liu, A. K. Engstfeld, S. Horch, B. Seger, I. E. L. Stephens, K. Chan, C. Hahn, J. K. Nørskov, T. F. Jaramillo and I. Chorkendorff, *Chem. Rev.*, 2019, **119**, 7610–7672.

21 H. A. Hansen, J. B. Varley, A. A. Peterson and J. K. Nørskov, *J. Phys. Chem. Lett.*, 2013, **4**, 388–392.

22 X. Liu, J. Xiao, H. Peng, X. Hong, K. Chan and J. K. Nørskov, *Nat. Commun.*, 2017, **8**, 15438.

23 H.-R. "Molly" Jhong, S. Ma and P. J. Kenis, *Curr. Opin. Chem. Eng.*, 2013, **2**, 191–199.

24 J. H. Golbeck, Ed., *Photosystem I*, Springer Netherlands, Dordrecht, 2006, vol. 24.

25 R. J. Spreitzer and M. E. Salvucci, *Annu. Rev. Plant Biol.*, 2002, **53**, 449–475.

26 C. A. Huff and M. S. Sanford, *J. Am. Chem. Soc.*, 2011, **133**, 18122–18125.

27 X. Wang, Z. Li, J. Shi, H. Wu, Z. Jiang, W. Zhang, X. Song and Q. Ai, *ACS Catal.*, 2014, **4**, 962–972.

28 K. D. Yang, C. W. Lee, K. Jin, S. W. Im and K. T. Nam, *J. Phys. Chem. Lett.*, 2017, **8**, 538–545.

29 K. Sun, T. Cheng, L. Wu, Y. Hu, J. Zhou, A. Maclennan, Z. Jiang, Y. Gao, W. A. Goddard and Z. Wang, *J. Am. Chem. Soc.*, 2017, **139**, 15608–15611.

30 Z. B. Hoffman, T. S. Gray, K. B. Moraveck, T. B. Gunnoe and G. Zangari, *ACS Catal.*, 2017, **7**, 5381–5390.

31 Y. Lum and J. W. Ager, *Energy Environ. Sci.*, 2018, **11**, 2935–2944.

32 E. L. Clark, C. Hahn, T. F. Jaramillo and A. T. Bell, *J. Am. Chem. Soc.*, 2017, **139**, 15848–15857.

33 H. Mistry, R. Reske, P. Strasser and B. Roldan Cuenya, *Catal. Today*, 2017, **288**, 30–36.

34 S. Ma, M. Sadakiyo, M. Heima, R. Luo, R. T. Haasch, J. I. Gold, M. Yamauchi and P. J. A. Kenis, *J. Am. Chem. Soc.*, 2017, **139**, 47–50.

35 Z. Chang, S.-J. Huo, W. Zhang, J. Fang and H. Wang, *J. Phys. Chem. C*, 2017, **121**, 11368–11379.

36 Y. Wang, D. Wang, C. J. Dares, S. L. Marquard, M. V. Sheridan and T. J. Meyer, *Proc. Natl. Acad. Sci.*, 2018, **115**, 278–283.

37 C. G. Morales-Guio, E. R. Cave, S. A. Nitopi, J. T. Feaster, L. Wang, K. P. Kuhl, A. Jackson, N. C. Johnson, D. N. Abram, T. Hatsukade, C. Hahn and T. F. Jaramillo, *Nat. Catal.*, 2018, **1**, 764–771.

38 W. Luo, W. Xie, R. Mutschler, E. Oveisi, G. L. De Gregorio, R. Buonsanti and A. Züttel, *ACS Catal.*, 2018, **8**, 6571–6581.

39 M. Jouny, W. Luc and F. Jiao, *Nat. Catal.*, 2018, **1**, 748–755.

40 N. Theaker, J. M. Strain, B. Kumar, J. P. Brian, S. Kumari and J. M. Spurgeon, *Electrochim. Acta*, 2018, **274**, 1–8.

41 Gurudayal, D. Perone, S. Malani, Y. Lum, S. Haussener and J. W. Ager, *ACS Appl. Energy Mater.*, 2019, **2**, 4551–4559.

42 Gurudayal, J. W. Beeman, J. Bullock, H. Wang, J. Eichhorn, C. Towle, A. Javey, F. M. Toma, N. Mathews and J. W. Ager, *Energy Environ. Sci.*, 2019, **12**, 1068–1077.

43 J. D. Goodpaster, A. T. Bell and M. Head-Gordon, *J. Phys. Chem. Lett.*, 2016, **7**, 1471–

1477.

44 C.-T. Dinh, T. Burdyny, M. G. Kibria, A. Seifitokaldani, C. M. Gabardo, F. P. García de Arquer, A. Kiani, J. P. Edwards, P. De Luna, O. S. Bushuyev, C. Zou, R. Quintero-Bermudez, Y. Pang, D. Sinton and E. H. Sargent, *Science*, 2018, **360**, 783–787.

45 E. L. Warren, W. E. McMahon, M. Rienäcker, K. T. VanSant, R. C. Whitehead, R. Peibst and A. C. Tamboli, *ACS Energy Lett.*, 2020, **5**, 1233–1242.

46 Y. Chen, C. W. Li and M. W. Kanan, *J. Am. Chem. Soc.*, 2012, **134**, 19969–19972.

47 C. W. Li, J. Ciston and M. W. Kanan, *Nature*, 2014, **508**, 504–507.

48 S. Essig, C. Allebé, T. Remo, J. F. Geisz, M. A. Steiner, K. Horowitz, L. Barraud, J. S. Ward, M. Schnabel, A. Descoeudres, D. L. Young, M. Woodhouse, M. Despeisse, C. Ballif and A. Tamboli, *Nat. Energy*, 2017, **2**, 17144.

49 Z. Lyu, S. Zhu, M. Xie, Y. Zhang, Z. Chen, R. Chen, M. Tian, M. Chi, M. Shao and Y. Xia, *Angew. Chemie*, 2021, **133**, 1937–1943.

50 R. H. Coridan, A. C. Nielander, S. A. Francis, M. T. McDowell, V. Dix, S. M. Chatman and N. S. Lewis, *Energy Environ. Sci.*, 2015, **8**, 2886–2901.

51 T. Reda, C. M. Plugge, N. J. Abram and J. Hirst, *Proc. Natl. Acad. Sci.*, 2008, **105**, 10654–10658.